Available online at www.sciencedirect.com
ScienceDirect
Journal of Inorganic Biochemistry 101 (2007) 375–384
Journal of Inorganic Biochemistry
www.elsevier.com/locate/jinorgbio

Observation of terahertz vibrations in *Pyrococcus furiosus* rubredoxin *via* impulsive coherent vibrational spectroscopy and nuclear resonance vibrational spectroscopy – interpretation by molecular mechanics

Ming-Liang Tan [d], Anna Rita Bizzarri [e], Yuming Xiao [a], Salvatore Cannistraro [e,*], Toshiko Ichiye [d], Cristian Manzoni [f], Giulio Cerullo [f], Michael W.W. Adams [c], Francis E. Jenney Jr. [c], Stephen P. Cramer [a,b,*]

[a] *Department of Applied Science, University of California, Davis, CA 95616, United States*
[b] *Physical Biosciences Division, Lawrence Berkeley National Laboratory, Berkeley, CA 94720, United States*
[c] *Department of Biochemistry and Molecular Biology, University of Georgia, Athens, GA 30602, United States*
[d] *Department of Chemistry, Georgetown University, Georgetown, MD 20057-1227, United States*
[e] *Biophysics and Nanoscience Center, INFM-CNISM, Universita' della Tuscia, I-01100 Viterbo, Italy*
[f] *National Laboratory for Ultrafast and Ultraintense Optical Science-CNR-INFM, Dipartimento di Fisica, Politecnico di Milano, Piazza Leonardo da Vinci 32, I-20133 Milano, Italy*

Received 7 April 2006; received in revised form 28 September 2006; accepted 29 September 2006
Available online 20 October 2006

Abstract

We have used impulsive coherent vibrational spectroscopy (ICVS) to study the $Fe(S\text{-}Cys)_4$ site in oxidized rubredoxin (Rd) from *Pyrococcus furiosus* (*Pf*). In this experiment, a 15 fs visible laser pulse is used to coherently pump the sample to an excited electronic state, and a second <10 fs pulse is used to probe the change in transmission as a function of the time delay. *Pf*Rd was observed to relax to the ground state by a single exponential decay with time constants of ~255–275 fs. Superimposed on this relaxation are oscillations caused by coherent excitation of vibrational modes in both excited and ground electronic states. Fourier transformation reveals the frequencies of these modes.

The strongest ICV mode with 570 nm excitation is the symmetric Fe–S stretching mode near 310 cm^{-1}, compared to 313 cm^{-1} in the low temperature resonance Raman. If the rubredoxin is pumped at 520 nm, a set of strong bands occurs between 20 and 110 cm^{-1}. Finally, there is a mode at ~500 cm^{-1} which is similar to features near 508 cm^{-1} in blue Cu proteins that have been attributed to excited state vibrations.

Normal mode analysis using 488 protein atoms and 558 waters gave calculated spectra that are in good agreement with previous nuclear resonance vibrational spectra (NRVS) results. The lowest frequency normal modes are identified as collective motions of the entire protein or large segments of polypeptide. Motion in these modes may affect the polar environment of the redox site and thus tune the electron transfer functions in rubredoxins.

Keywords: Rubredoxin; *Pyrococcus furiosus*; Normal mode; Impulsive coherent vibrational spectroscopy

1. Introduction

Rubredoxins, with a single $Fe(S\text{-}Cys)_4$ redox center, are among the smallest (~50 amino acid) and simplest electron

* Corresponding authors. Tel.: +1 530 752 0360; fax: +1 530 752 2444 (S.P. Cramer).
E-mail addresses: cannistr@unitus.it (S. Cannistraro), spcramer@lbl.gov (S.P. Cramer).

0162-0134/$ - see front matter © 2006 Elsevier Inc. All rights reserved.
doi:10.1016/j.jinorgbio.2006.09.031

transfer proteins [1]. They are key electron donors in alkane oxidation pathways [2] and in superoxide reduction [3]. Apart from their biological significance, rubredoxins have often been employed as model systems for the development of spectroscopic techniques such as resonance Raman spectroscopy [4,5], EXAFS [6], L-edge spectroscopy [7], X-ray magnetic circular dichroism – XMCD [8], high-resolution X-ray fluorescence [9], resonance energy transfer – RET [10], optically detected electron paramagnetic resonance – ODEPR [11], and nuclear resonance vibrational spectroscopy – NRVS [12], that are ultimately employed on more complex metalloproteins. Rubredoxin from *Pyrococcus furiosus* (*Pf*Rd), the object of the current study, has an unfolding rate of $\sim 10^{-6}\ s^{-1}$ at 100 °C [13] and has served as a model for structural features underlying thermal stability in hyperthermophilic proteins. An assortment of experimental [13,14] and computational [15] investigations has examined *Pf*Rd large-scale dynamical properties with respect to both high temperature stability and the unusual temperature dependence of its redox potential. The redox potential is about 0 mV at 25 °C and changes to ~160 mV at 90 °C at pH 8.0. Despite this wealth of studies, questions remain about its conformational flexibility, especially in regard to motion that could affect its electron transfer properties.

The structure of *Pf*Rd has been characterized by X-ray diffraction at 0.95 Å resolution (1BRF) [16], by neutron diffraction at 1.5 Å (1VCX) [17], and in solution by NMR [18]. The approximately tetrahedral FeS_4 site has been described as approaching D_{2d} symmetry *via* compression along an S_4 axis (Chart 1). This distortion is exhibited in part as two shorter Fe–S bond lengths (2.25–2.26 Å) (Fe–SCys8 and Fe–SCys41) and two slightly longer Fe–S bonds (2.28–2.30 Å) (Fe–SCys5 and Fe–SCys38).

In this paper, we study the vibrational dynamics of oxidized *Pf*Rd using impulsive coherent vibrational spectroscopy (ICVS). This is a technique enabling direct time-domain observation of the vibrational modes coupled to an electronic transition. It involves pumping an optical transition in the sample with a short (~10 fs) pulse of sufficient intensity to drive a fraction of the molecules of interest into the excited state, and then monitoring the pump-induced transmission changes with a suitably delayed short probe pulse. If the pump pulse has a duration significantly shorter than the periods of the vibrations of interest, it projects the ground-state multidimensional vibrational wave function onto the excited state in the form of a vibrational wave packet [19,20]. Periodic motion of the localized packet formed in this way along displaced bond coordinates modulates in time the molecular absorption, which is measured by the probe pulse. Details of the ICVS theory have been explained elsewhere [21,22].

ICVS has particular strengths with respect to other vibrational techniques – it enables direct time-domain observation of low frequency vibrational modes that are difficult to observe by far-infrared or Raman spectroscopies, it provides information on excited state vibrational modes which are not accessed by resonance Raman, and it is relatively insensitive to interference from fluorescent contaminants or solvent bands. ICVS has already been applied to heme proteins [23,24], green fluorescent protein [25], and blue copper proteins such as azurin [26] and plastocyanin [27].

In this paper, we report on the real-time vibrational dynamics of oxidized *Pf*Rd pumped at 520 or 570 nm and probed at several different wavelengths. The ICV spectra extend to lower frequencies than typical metalloprotein resonance Raman spectra, revealing modes never seen before in Fe–S proteins, but similar to those seen in blue Cu proteins [27,28] and in heme proteins by inelastic neutron scattering [29]. Normal mode calculations that include the entire protein as well as solvent water are used to interpret the experimental spectra. These calculations can be used to explain both the current ICVS observations and to quantitatively reproduce the recently reported NRVS data [12]. The results are also compared with previous Raman and molecular mechanics analyses of rubredoxins.

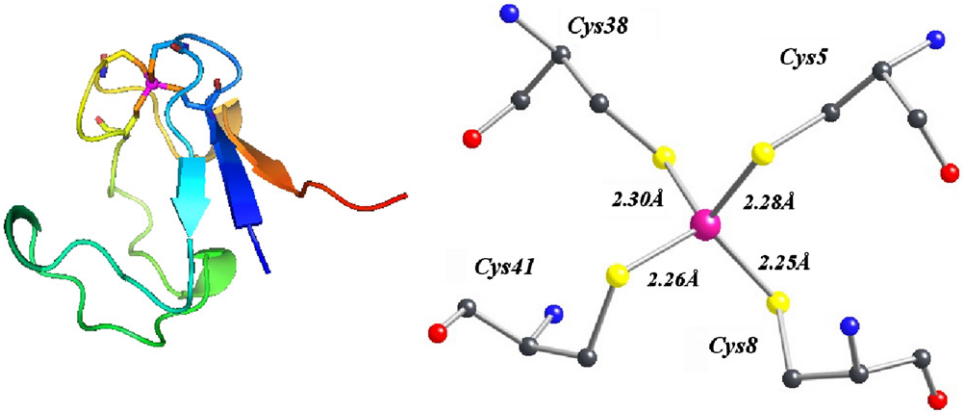

Chart 1. Left: A ribbon diagram for oxidized *Pf*Rd, including sticks for cysteine side chains, illustrating location of Fe site (purple) with respect to three beta sheets and two loops. Right: Close-up of Fe site showing compression of Fe–SCys8 and Fe–SCys41 bonds (PDB code 1BRF) [16]. (For interpretation of the references in colour in this figure legend, the reader is referred to the web version of this article.)

2. Experimental

2.1. Protein purification and sample preparation

*Pf*Rd was purified by published procedures and concentrated to 12 mg/ml for shipping [30]. The protein was diluted to give an absorbance of 0.31 at 490 nm in a Tris buffer at pH 8. The ICVS measurements used 0.5 mm pathlength quartz cuvettes.

2.2. Impulsive coherent vibrational spectroscopy

ICVS time traces were recorded at room temperature using published procedures [27] at the National Laboratory for Ultrafast and Ultraintense Optical Science (Milano, Italy). The experimental setup starts with an amplified Ti:sapphire laser (500 μJ, 150 fs, 1 kHz) driving two non-collinear optical parametric amplifiers (NOPAs). The first NOPA generates transform-limited 15 fs pulses tunable in the visible (500–700 nm); the second NOPA generates ultra-broadband visible pulses (500–700 nm bandwidth) compressed to nearly transform-limited sub-10 fs duration by chirped dielectric mirrors. The pulses derived from the NOPAs are synchronized by a delay line and focused on the sample using only reflective optics, in a standard non-collinear pump-probe configuration. An intense pulse from the first NOPA, serves as the pump, while a weaker, delayed pulse from the second NOPA probes the differential transmission changes ($\Delta T/T$). For the current experiments, the pump pulse was tuned to either 520 or 570 nm and the relative polarization of the pump and probe beams was set to 90° in order to reduce the artifact at zero time delay due to the buffer. Time-resolved measurements at specific wavelengths were obtained by selecting, after the sample, spectral components of the broadband probe pulse with 10 nm bandwidth interference filters. To increase the signal-to-noise ratio, the pump pulse was mechanically modulated by a chopper and the probe pulse signal, detected by a slow photodiode, was directed to a lock-in amplifier, locked to the modulation frequency of the chopper. In this manner, only pump-induced changes of the transmitted probe energy are detected. In addition, to remove intrinsic probe pulse energy fluctuations, a differential detection scheme was adopted. A replica of the probe pulse that crossed an unpumped region of the sample was sent to a photodiode identical to that used for probe pulse detection. An electronic signal proportional to ΔT was obtained by subtracting the photodiode output signals in a differential amplifier before lock-in detection.

In order to obtain the absolute value of the $\Delta T/T$ signal, the voltage reading from the lock-in amplifier was divided by the probe voltage signal, measured by an oscilloscope, and the result was multiplied by the appropriate conversion factor. This factor was obtained by measuring with the lock-in a known signal (100% $\Delta T/T$) – obtained by blocking the probe pulse with the chopper. In all measurements, excitation intensity was kept in the linear regime, with $\Delta T/T$ below 2–3%. Absorption spectra of *Pf*Rd were taken immediately before and immediately after the pump-probe measurements to check that no sample degradation occurred.

2.3. Normal mode calculations

The high-resolution crystal structure (0.95 Å) of oxidized wild-type *Pf*Rd with crystal water was obtained from the Protein Data Bank 1BRF [16]. The hydrogen positions were built for all polar hydrogens using the HBUILD facility of CHARMM 29 [31]. All non-polar hydrogens were treated *via* the extended atom model as part of the heavier atom to which they are attached. The system contains 488 protein atoms and 558 crystal water molecules. The force field parameters consisted of the CHARMM19 parameters [31] plus additional parameters for the $Fe–S_4$ site as described elsewhere [32].

The system was energy-minimized by 1000 steps of steepest descent method followed by 5570 steps of the adopted basis Newton–Raphson (ABNR) method; the minimization was terminated when the rms energy gradient was reduced to 10^{-7} kcal/mol/Å. The normal mode calculations were performed with the VIBRan module in the CHARMM program [31]. For a given mode α, the mode composition factor $e^2_{j\alpha}$ of atom j was calculated by [33–35]:

$$e^2_{j\alpha} = \frac{m_j r^2_{j\alpha}}{\sum_j m_j r^2_{j\alpha}} \quad (1)$$

where m_j and $r_{j\alpha}$ are the mass of atom j and its eigenvector in mode α respectively. For comparison with the experimental spectra, Gaussian functions were calculated centered around each ω_α, the frequency of mode α, using an 8 cm^{-1} full width at half maximum and an amplitude proportional to $e^2_{j\alpha}$. The partial vibrational density of states for atom j was then obtained by summing these Gaussian functions over all modes.

3. Results

*Pf*Rd solutions were investigated by pump-probe experiments resonant with the S → Fe ligand-to-metal charge-transfer (LMCT) transitions, using 15 fs pump pulses centred at either 520 or 570 nm. For both pump wavelengths, different probe wavelengths (from 480 to 700 nm) of the ultra-broadband probe pulse were analyzed. Fig. 1 shows the ground-state absorption spectrum of *Pf*Rd together with the spectra of pump and probe pulses.

The time evolutions of the differential transmission ($\Delta T/T$) signals, obtained by exciting with a pump wavelength of 570 nm and probing at 540 nm, or pumping at 520 nm and probing at 560 nm, are shown in the insets of Fig. 2. The signals exhibit a strong spike at zero time delay that lasts for about 50 fs; this is due to a non-resonant response by the buffer solution [27]. The $\Delta T/T$ signals, starting from the delay time for which the buffer response has ceased, are also shown in Fig. 2. An exponential decay, modulated

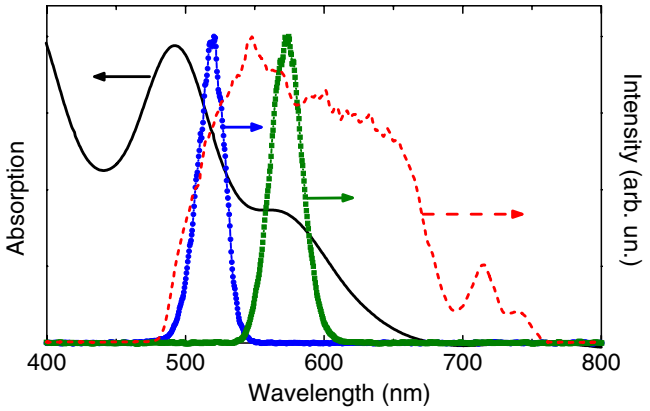

Fig. 1. Absorption spectrum for oxidized *Pf*Rd (—), compared with ultra-broadband sub-10 fs probe pulse (– – –). Pump pulses used for excitation at 520 nm (–●–) and 570 nm (–■–) are also shown.

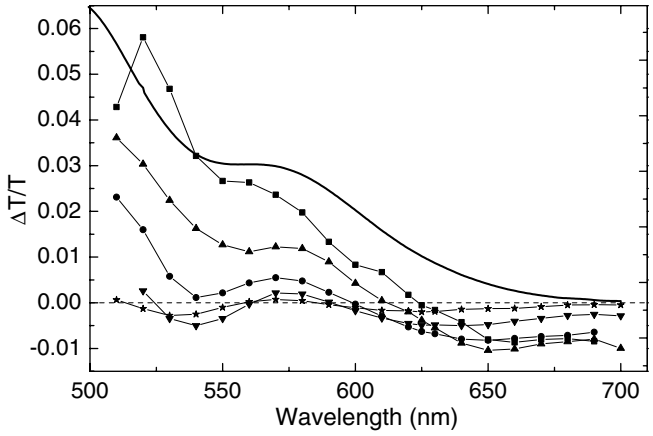

Fig. 3. Absorption spectrum for oxidized *Pf*Rd (—), compared with $\Delta T/T$ spectra taken with a pump at 570 nm at different pump-probe delays: 100 fs (■), 200 fs (▲), 500 fs (●), 1000 fs (▼), 2000 fs (★).

by clearly visible oscillations, is observed in both cases. The transmission increase, ascribed to photobleaching (PB) of the LMCT transition, decays exponentially as a consequence of the recovery of the ground-state population. Superimposed on this decay are oscillatory components, assigned to vibrational coherence in the excited and ground states, created by the very short pump pulses [36].

Let us first describe the population dynamics. By fitting the $\Delta T/T$ data with an exponential plus a constant offset, we found time constants of ~275 and ~255 fs for ground-state recovery using 570 or 520 nm pump excitation, respectively. These time constants are similar to the ~230–300 fs values measured in blue copper proteins such as plastocyanin and azurin [26,27,36,37], suggesting that strong non-radiative coupling between ground and excited states is a general characteristic of electron transfer proteins.

Fig. 2a shows the $\Delta T/T$ dynamics at 540 nm probe wavelength (with excitation centered at 570 nm). We note that over longer times, the $\Delta T/T$ signal does not return to zero, but in fact changes sign, giving rise to a weak photoinduced absorption (PA) signal. This PA lives longer than the PB and decays in about 600 fs. The appearance of a broad PA band at long delays is clearly visible from the $\Delta T/T$ spectra at different pump-probe delays (Fig. 3). It can be seen that this PA rises promptly in the red (630–700 nm), while it appears in the blue only after ~1 ps. One possible explanation for this signal is a partial decay of the population from one excited state to another state where it lives for a longer time. Absorption by molecules in this new state could give rise to the PA signal. Alternatively, it might be due to the formation of a vibrationally hot ground state, following the ultrafast internal conversion process. The population of higher-lying vibrational levels in the ground state would give rise to a transient absorption signal which is red-shifted with respect to the equilibrium ground-state absorption, thus explaining the PA tail in the red. Fig. 4 shows the oscillatory component of these signals, after the slowly varying population dynamics has been subtracted, and the Fourier transforms of these curves are shown in Fig. 5.

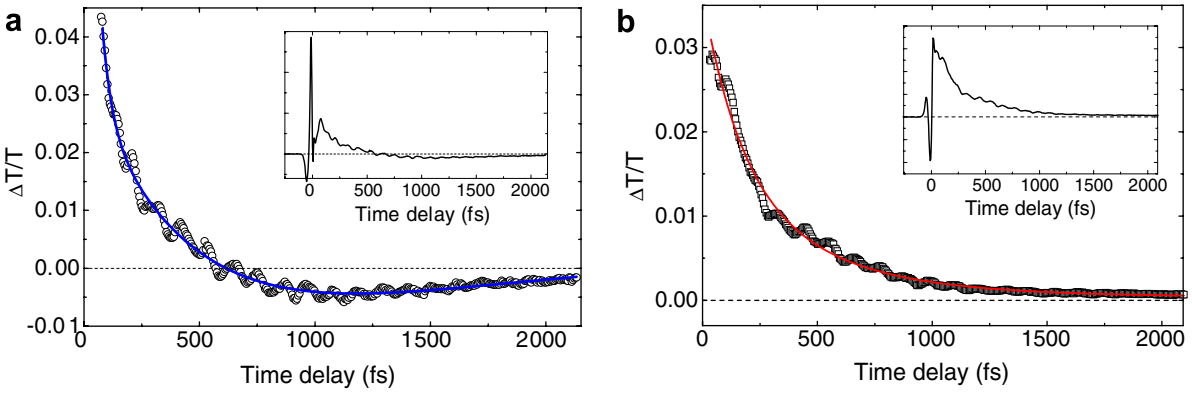

Fig. 2. $\Delta T/T$ traces for oxidized *Pf*Rd taken with (a) pump at 570 nm and the probe at 540 nm and (b) pump at 520 nm and the probe at 560 nm. Experimental data (dots) and fits with exponential plus constant offset (continuous lines). Insets show the full-scale experimental signals with the buffer-induced artifact.

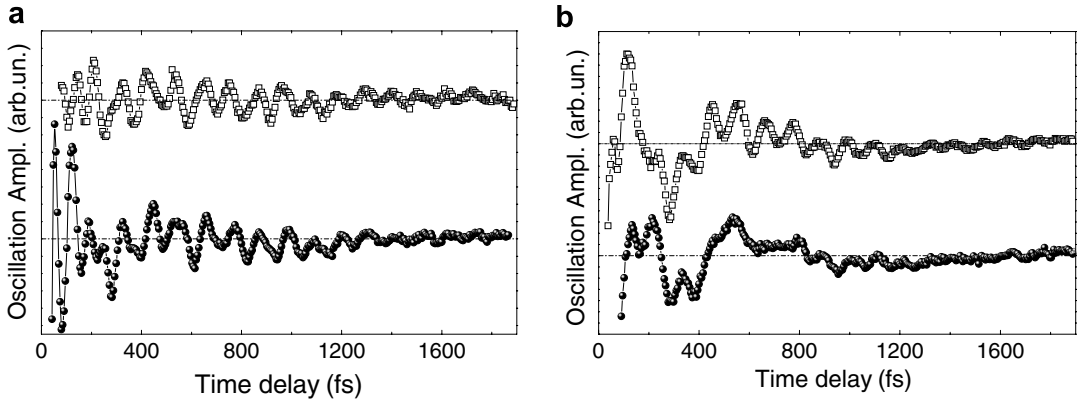

Fig. 4. Oscillatory component of the $\Delta T/T$ signal for oxidized *Pf*Rd: (a) pump at 570 nm and probe at 540 (top) or 570 nm (bottom); (b) pump at 520 nm and probe at 560 (top) or 580 nm (bottom).

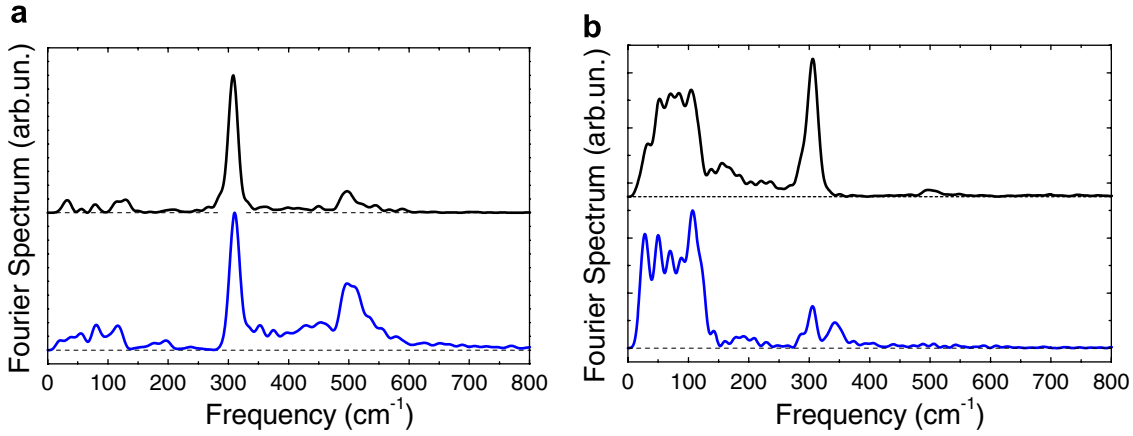

Fig. 5. Fourier transforms of the oscillatory components of signals shown in Fig. 4: (a) pump at 570 nm and probe at 540 (top) or 570 nm (bottom); (b) pump at 520 nm and probe at 560 (top) and 580 nm (bottom).

3.1. Fe–S stretching modes

In all cases, a strong peak at ~310 cm^{-1} is observed in the Fourier transform. This presumably corresponds to the dominant band seen at ~313 cm^{-1} in the resonance Raman spectrum of a frozen *Pf*Rd solution [12]. In the latter spectrum, the associated normal mode has been approximately described as the totally symmetric stretch of the $Fe(S\text{-}Cys)_4$ site. With 520 nm excitation and 580 nm detection, a peak at ~342 cm^{-1} appears that can be related to the asymmetric Fe–S stretching modes seen at ~347 cm^{-1} [12]. With 570 nm excitation and 570 nm detection, another band appears at ~374 cm^{-1}, which nicely matches the Fe–S asymmetric stretch seen at ~374 cm^{-1} in the resonance Raman data [12]. The remaining Fe–S asymmetric stretch at 362 cm^{-1}, which is the strongest asymmetric stretch in the 568 nm resonance Raman, is barely perceptible in the 570 nm pump/570 nm probe data.

3.2. High frequency features

In addition to the Fe–S stretching modes, a peak at ~500 cm^{-1} is also present, especially for the 570 nm pump wavelength. The ~500 cm^{-1} band is broad and trails toward higher energy. There are no strong peaks in the resonance Raman in this region (although very weak bands at 502 and 518 cm^{-1} were reported without assignment by Czernuszewicz et al. [38]). Features between 500 and 510 cm^{-1} have been previously observed in the ICVS of other electron transfer proteins, such as plastocyanin, ceruloplasmin, and azurin [26,27,36].

Additional insight into the nature of this feature can be obtained from the spectrogram obtained *via* a sliding window Fourier transform (SWFT) of the oscillatory component of the signal [39,40]. This is essentially a series of Fourier transforms carried out on different time windows with position swept along the whole measurement domain. The SWFT is obtained according to the formula:

$$S(\omega,\tau) = \int_0^\infty s(t)g(t-\tau)\exp(-i\omega t)dt \qquad (2)$$

where $s(t)$ is the oscillatory component of the signal and $g(t-\tau) = \exp[-(t-\tau)/t_p]^n$ is a super-Gaussian window function. A SWFT spectrum for the trace using a 570 nm probe wavelength is shown in Fig. 6. It indicates a damping time of 250–350 fs for the 500 cm^{-1} mode and 1000 fs

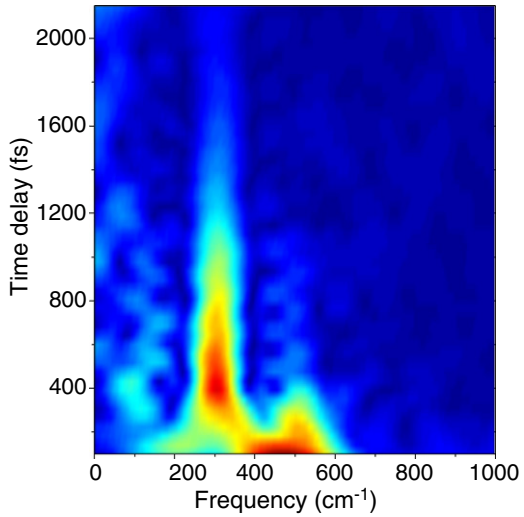

Fig. 6. Spectrogram obtained by performing the SWFT of the oscillatory component of the signal at 570 nm probe wavelength. The calculation used $n = 6$ and $\tau_p = 70$ fs.

for the 310 cm^{-1} mode. The coincidence between damping time and excited state lifetime suggests assigning the ~500 cm^{-1} mode to the excited state of the LMCT transition. The longer damping for the ~310 cm^{-1} mode indicates that it derives from a ground-state coherence effect.

The origin of the 500 cm^{-1} mode deserves further discussion. It cannot be attributed to the solvent – water does not have any Raman peak at this frequency, and a pump-probe experiment on the pure solvent did not reveal any such oscillation. Both the fast damping time and the absence in the resonance Raman spectrum suggest assignment to an excited state. In blue Cu proteins, a line at approximately the same frequency has also been attributed to excited state vibrations [27,36].

3.3. Low frequency modes

One strength of ICVS, as a time-domain technique, is the ability to see low frequency features that are outside the range of typical protein resonance Raman or FT–IR experiments. In all of the spectra, low frequency oscillations below 200 cm^{-1} are clearly visible in the Fourier transforms. The bands between 100 and 200 cm^{-1} can be expected to have significant S–Fe–S bending motion, and have been seen in previous resonance Raman work [38] and NRVS studies [12]. There are also strong features below 100 cm^{-1}, which presumably involve more extended motion of the chromophore and protein matrix. Before we consider these modes in detail, we note that little work has been done on such modes in rubredoxin, and the degree of direct coupling between large-scale protein modes and localized charge-transfer transitions, such as the current S → Fe transitions involved in rubredoxin, is still the subject of considerable debate. In contrast, there have been a number of studies regarding low frequency 'protein modes' in both heme proteins and in blue Cu proteins.

For example, in pump-probe experiments involving myoglobin–CO photolysis, Miller and coworkers observed peaks as 25, 48, 84, and 134 cm^{-1}, along with common higher frequency heme modes [41,42]. The lowest two peaks were respectively assigned to a heme doming mode and to longer-range motions involving isopropyl side chains. Miller et al. argue for coupling between localized, high frequency modes near the porphyrin center and more extended modes involving the entire heme, which in turn couple to low frequency collective modes such as those that involve motion of the myoglobin E–F helix. Rosca et al. also observed modes around 20 cm^{-1} in a variety of heme-protein samples [24].

Blue copper proteins have been extensively studied by pump-probe techniques. Book and coworkers used 16 fs 770 nm pumping of the d–d transitions to observe modes in the 35–55 cm^{-1} region in plastocyanins and ceruloplasmin; they attributed these to protein 'phonon' modes [36]. By pumping the S → Cu LMCT band with 10 fs 550 nm pulses, similar features at 22, 50, and 75 cm^{-1} were seen in poplar plastocyanin by Cimei et al., who invoked 'collective modes involving large biomolecule regions' [27]. Nakashima et al. observed a band in *Synechococcus* plastocyanin at ~33 cm^{-1}; they attributed the most likely assignment to a "delocalized one that includes the protein skeleton motion" [43]. In azurin, features at ~30, 55 and 80 cm^{-1} have been observed by ICVS [26] and inelastic neutron scattering spectroscopes [44], where the lowest energy mode was referred to a 'boson peak'. There has been speculation that low frequency modes might be relevant to the electron transfer process during interaction with physiological partners [45].

In the current case of rubredoxin, the relative intensity of the <100 cm^{-1} modes compared to the 310 cm^{-1} Fe–S stretch varies considerably with both pump and probe wavelength. Both of the absorption features used in this study have been attributed to S → Fe charge-transfer excitations, but with different polarization [46]. Specifically, the ~560 nm band has been assigned as a *z*-polarized $^6A_1 \rightarrow {}^6B_2$ transition, while the 490 nm band has been assigned as primarily *xy*-polarized $^6A_1 \rightarrow {}^6E$ [47]. The relative intensities may be related to the directions within the protein along which excitations are induced and monitored.

The weakest low frequency effects are seen with 570 nm excitation and 540 nm detection, where the low frequency modes have ~10% of the intensity of the 310 cm^{-1} band. Nevertheless clear features at ~32, 56, and 78 cm^{-1} are observed. With 520 nm excitation and 560 nm detection, the low and high frequency bands have comparable intensity, and features are seen at ~32, 52, 70, 84, and 105 cm^{-1}. Finally, with 520 nm excitation and 580 nm detection, the low frequency modes dominate, with clear features at 28, 50, and 70 cm^{-1}, as well as additional modes at 88 and 105 cm^{-1}. We note that the 28–32 cm^{-1} intensity that is

seen in all the ICVS data may be related to a 34 cm^{-1} shoulder that is seen in the NRVS [12].

3.4. Normal mode analysis

In order to better understand the nature of the low frequency modes that contribute to the ICVS and NRVS signals, we conducted a normal mode analysis using Fe, all of the amino acid residues, and 558 waters. There are 3132 vibration normal modes. Fig. 7 shows the calculated normal mode spectrum of *Pf*Rd for frequencies up to 1800 cm^{-1}. The overall trend is similar to previous results for bovine trypsin inhibitor [48].

The quantitative simulation of ICVS spectra is beyond the scope of this work; we chose instead to focus on comparison with the NRVS data, where calculation of the signal amplitude is straightforward [33–35]. The first 1562 vibrational modes, with highest frequency of 600 cm^{-1}, were used to calculate the ^{57}Fe PVDOS, since the mode composition factor $e^2_{j\alpha}$ is essentially zero for modes with frequency higher than 550 cm^{-1}. The contribution of each mode to the simulation spectra was weighted by $e^2_{j\alpha}$, as indicated in Eq. (1). To compare the theoretical results with experiment, the PVDOS for Fe and each of the four cysteine sulfurs at the Fe site were calculated (Figs. 8 and 9).

The calculated Fe-centered PVDOS can be directly compared with previous results from NRVS experiments [12] (Fig. 8). Three main regions can be distinguished – asymmetric Fe–S stretching around 350 cm^{-1}, asymmetric bending near ~120–200 cm^{-1}, and protein skeleton moving modes below 100 cm^{-1}. As shown in Fig. 8, the NMA using previous Fe–S force constants [32] yields reasonable overall agreement with the NRVS, despite a peak near ~150 cm^{-1} that is slightly too high in energy and a peak near ~350 cm^{-1} that is too low compared to the NRVS. These features are brought into line with the adjusted parameters: force constants $K_{Fe-S} = 1.25$ mdyne $Å^{-1}$ *vs.*

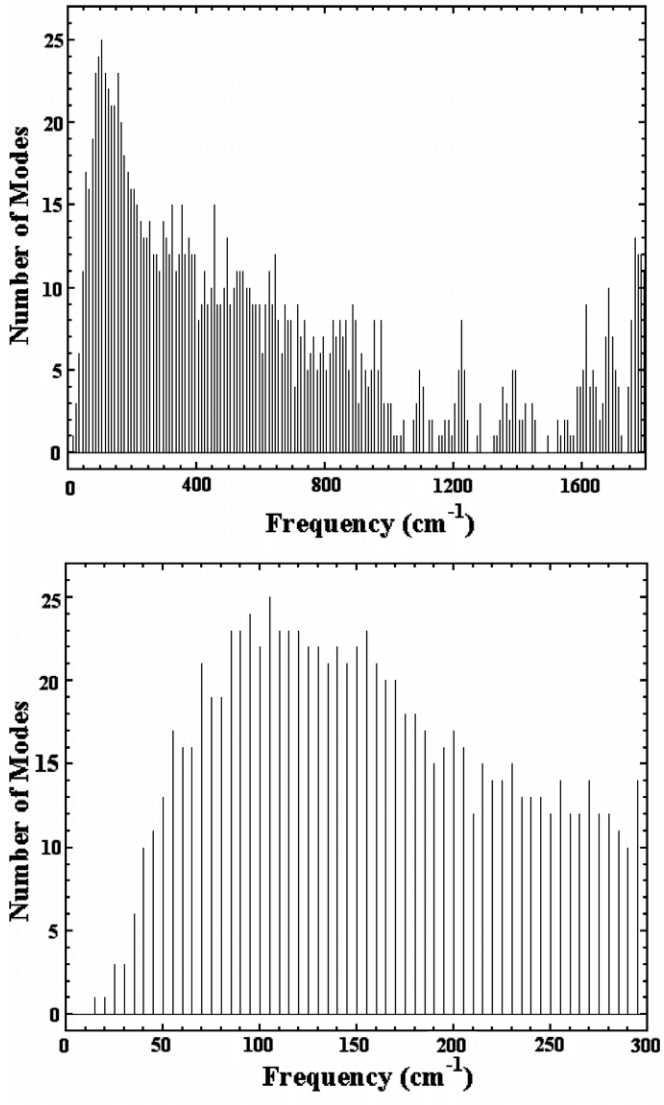

Fig. 7. Histogram of calculated normal mode frequencies for oxidized *Pf*Rd, constructed per 5 cm^{-1} interval.

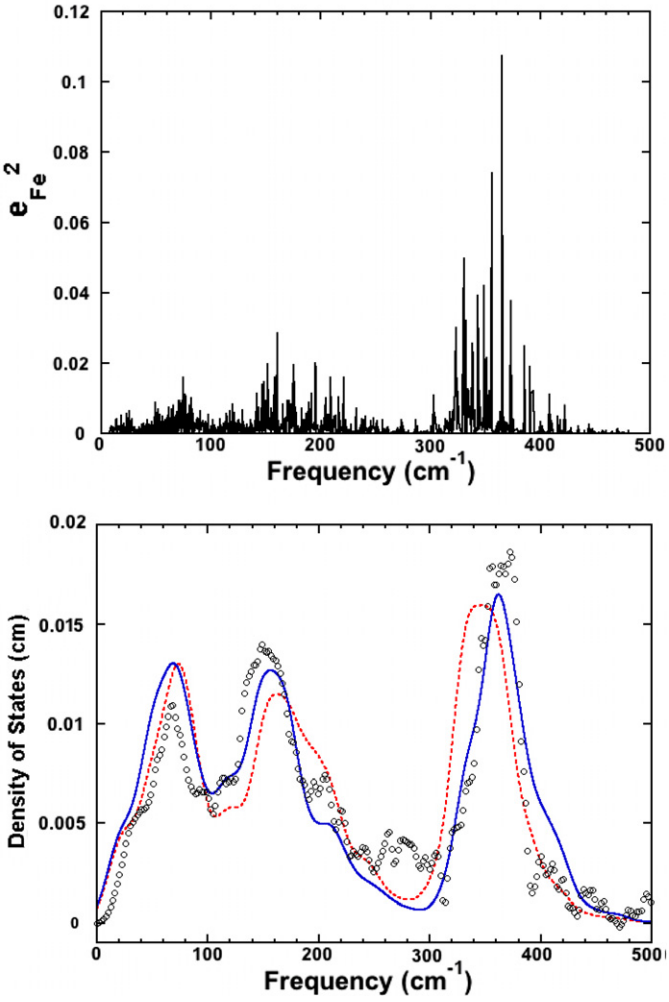

Fig. 8. Top – mode composition factors for Fe. Bottom – PVDOS for Fe (a) from NRVS experiment (○○○○), (b) calculated from NMA results using published force constants [32] (------), and (c) calculated using force constants refined in this work (—).

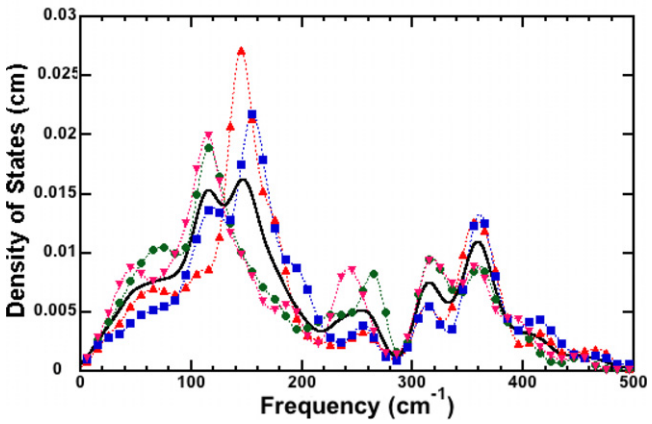

Fig. 9. Calculated PVDOS for (a) S in Cys5 (–▲–), (b) S in Cys8 (–●–), (c) S in Cys38 (–■–), (d) S in Cys41 (–▼–), and (e) 4 ligand sulfurs (—).

original 1.1 mdyne Å^{-1} and $H_{S–Fe–S} = 0.28$ mdyne Å^{-1} *vs.* 0.56 mdyne Å^{-1}, resulting in good agreement between the molecular mechanics normal mode calculation and the NRVS ^{57}Fe PVDOS spectra.

Of special interest for the current study are modes below 100 cm^{-1} (Figs. 7 and 8). The composition of these modes is illustrated in Figs. 8 and 9, while the detailed information about the direction and relative displacement of atoms is contained in calculated eigenvectors for each mode. Fig. 10 shows atomic motions involved in four specific low frequency modes. These were chosen because they have relatively large e^2_{Fe} value and thus contribute more to the calculated PVDOS (Fig. 8). The atomic motions, which involve concerted motion of a significant fraction of the protein, are shown in Fig. 10.

The lowest frequency modes, below 100 cm^{-1}, have not been interpreted before for rubredoxin. Modes between 20 and 80 cm^{-1} have been seen using ICVS techniques in blue Cu proteins such as azurin and plastocyanin [27], which are of comparable size. In these proteins, they have been referred to as 'phonon-like' [36] or as 'delocalized mode(s) involving the protein skeleton motion' [43]. In our calculations, some of these Rd modes involve concerted in-phase collective motion of large segments of polypeptide (Fig. 10). For the mode at 13 cm^{-1} (Fig. 10a), the concerted motion of the Fe cluster along with the nearby polypeptide is coupled to the concerted motion of loop-1 (residues 15–27) and loop-2 (residues 30–37), so that the two parts of the protein twist with respect to each other.

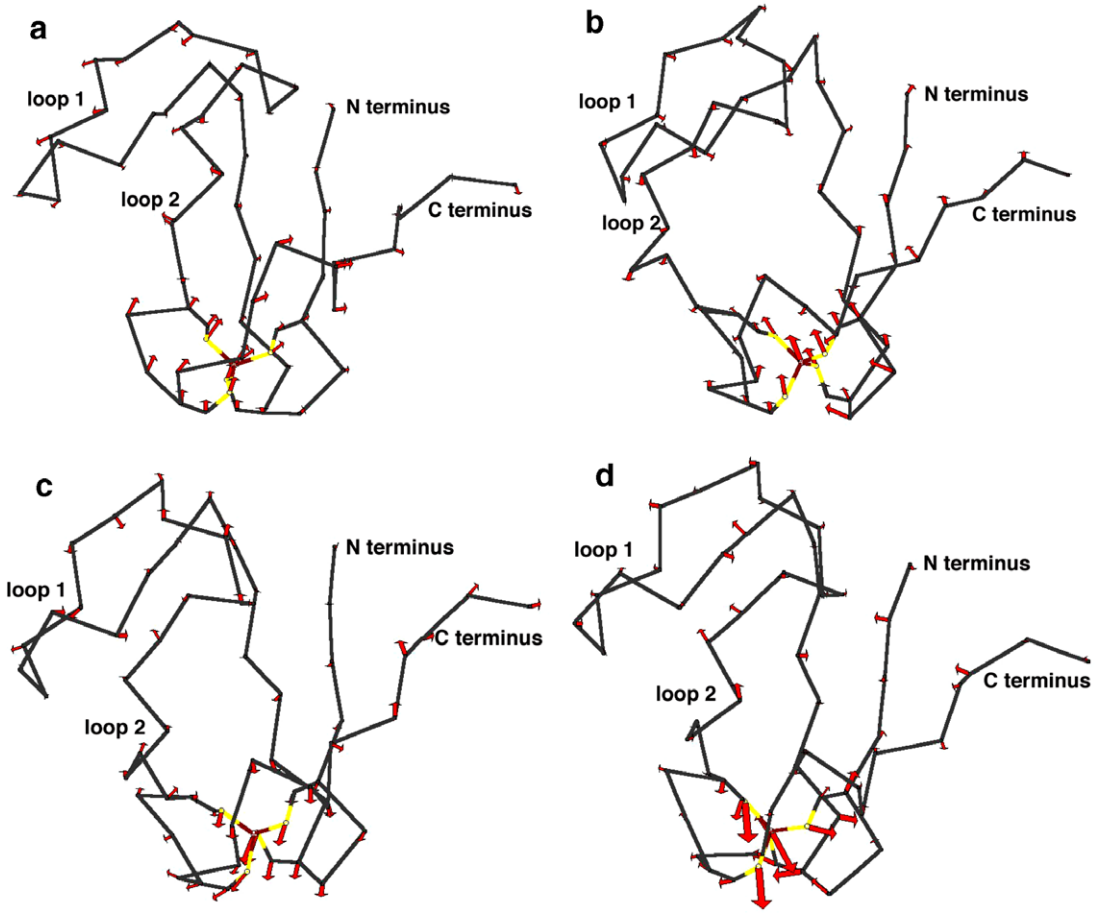

Fig. 10. Illustration of correlated protein motions involved in four normal modes. Arrows (rescaled between frames to enhance visibility) represent the relative directions and magnitudes of C_α atoms of the corresponding residues (residues 1–53) and Fe, S and C_β atoms in the redox site: (a) 13 cm^{-1}, (b) 18 cm^{-1}, (c) 28 cm^{-1}, and (d) 82 cm^{-1}.

For the mode at 18 cm^{-1} (Fig. 10b), the concerted motion of the Fe cluster along with the nearby polypeptide and the concerted motion of loop-2 are in opposite directions, indicating a stretching motion of the protein, while loop-1 twists with respect to the rest of the protein. In the 28 cm^{-1} mode (Fig. 10c), the Fe center with nearby polypeptide and C-terminus tail stretch in opposite directions. Finally for the mode at 82 cm^{-1} (Fig. 10d), the entire protein undergoes a right-hand twisting movement.

4. Discussion and conclusions

The experimental results from our study of *Pf*Rd reveal a variety of previously unobserved low frequency vibrational modes, below 100 cm^{-1}, that are observed in both the NRVS and ICVS data. The interpretation of these features has been assisted by a full protein normal mode analysis. Overall, these low frequency modes can be assigned to collective motion of the entire protein or to delocalized collective motion of large segments of polypeptide. These motions involve relative movement of the Fe–S active center along with nearby residues, loops, and protein N- or C-termini. Stretching or twisting motions of loop-1, loop-2 or either terminus in the lowest frequency modes will result in partial exposure of the polar backbone in the protein core to water. The different polar environments of the Fe–S active center that occur in different low frequency modes may affect the properties of the redox site and thus the function of the protein. It is interesting to note that motion of loop-1 and loop-2 in opposite directions shown in the 28 cm^{-1} mode is very similar to the movement observed before in molecular dynamics simulations [15,49].

In a previous normal mode calculation, Urushiyama and coworkers have argued that in rubredoxin [50], as well as ferredoxins [51], the Fe–S modes are 'extensively coupled to deformations of the polypeptide backbone'. Significant coupling of the Fe–S stretch with cysteine backbone deformations was also deduced from 1–2 cm^{-1} shifts after ^{15}N-labeling of the cysteine nitrogens [52]. Having now modeled the entire protein, we can address the extent of delocalization in the different normal modes. In our calculations we find that the asymmetric Fe–S stretching modes around 350 cm^{-1} contain the largest fractions of Fe kinetic energy, but there is always considerable motion of the entire cysteine residues. In contrast, the lowest frequency modes are delocalized over the entire protein. In general, the lower the frequency of the mode, the more delocalized is the motion in that mode.

In summary, we have reported the time-domain observation, using the ICVS technique, of the vibrational modes coupled to the LMCT transition in *Pf* rubredoxin. With this method, we observed bands down to 28 cm^{-1}. The lowest frequency normal modes can be described as delocalized collective skeletal motion involving large regions of the protein. These movements may be important in the unfolding of the polypeptide backbone and the electron transfer function of rubredoxins, suggesting that proteins may have low frequency modes that correlate with the specific physiological functions.

From the wavelength dependence of the observed spectra, we have found that ICVS is an information-rich technique that remains to be fully exploited. The ICVS experiment has special strengths for observation of low frequency large-scale protein modes, some of which may be important in the electron transfer process. Since it can be done on moderately dilute solutions, ICVS provides information about metalloproteins under physiologically relevant conditions. With the continuing development of sources of tunable femtosecond light pulses with duration down to a few optical cycles [53], ICVS should become a more routine technique that complements resonance Raman and infrared probes of biomolecular dynamics.

5. Abbreviations

ICVS	impulsive coherent vibrational spectroscopy
Rd	rubredoxin
Pf	*Pyrococcus furiosus*
NRVS	nuclear resonance vibrational spectroscopy
EXAFS	extended X-ray absorption fine structure
XMCD	X-ray magnetic circular dichroism
RET	resonance energy transfer
NMR	nuclear magnetic resonance
NOPA	non-collinear optical parametric amplifier
ABNR	adopted basis Newton–Raphson
LMCT	ligand-to-metal charge-transfer transition
PB	photobleaching
PA	photoinduced absorption
SWFT	sliding window Fourier transform
PVDOS	partial vibrational density of states
NMA	normal mode analysis

Acknowledgments

This work was funded by NIH Grants EB-001962 (SPC), GM-65440 (SPC), GM-60329 (MWWA), GM-45303 (TI), and the DOE Office of Biological and Environmental Research (SPC). This work has been partially supported by the FIRB-MIUR Project "Molecular Nanodevices" and a PRIN-MIUR 2004 project.

References

[1] J. Meyer, J.-M. Moulis, in: A. Messerschmidt, R. Huber (Eds.), Handbook of Metalloproteins, Wiley, New York, 2001, pp. 505–517.
[2] J.B.v. Beilen, M. Neuenschwander, T.H.M. Smits, C. Roth, S.B. Balada, B. Witholt, J. Bacteriol. 184 (2002) 1722–1732.
[3] F. Auchere, R. Sikkink, C. Cordas, P. Raleiras, P. Tavares, I. Moura, J. Biol. Inorg. Chem. 9 (2004) 839–849.
[4] T.V. Long, T.M. Loehr, J. Am. Chem. Soc. 92 (1970) 6384–6386.
[5] V.K. Yachandra, J. Hare, I. Moura, T.G. Spiro, J. Am. Chem. Soc. 105 (1983) 6455–6461.
[6] R.G. Shulman, P. Eisenberger, W.E. Blumberg, N.A. Stombaugh, Proc. Natl. Acad. Sci. 72 (1975) 4003–4007.

[7] S.J. George, J. van Elp, J. Chen, Y. Ma, C.T. Chen, J.B. Park, M.W.W. Adams, B.G. Searle, F.M.F. Degroot, J.C. Fuggle, S.P. Cramer, J. Am. Chem. Soc. 114 (1992) 4426–4427.
[8] J. van Elp, S.J. George, J. Chen, G. Peng, C.T. Chen, L.H. Tjeng, G. Meigs, H.J. Lin, Z.H. Zhou, M.W.W. Adams, B.G. Searle, S.P. Cramer, Proc. Natl. Acad. Sci. 90 (1993) 9664–9667.
[9] X. Wang, M.M. Grush, A.G. Froeschner, S.P. Cramer, J. Syn. Rad. 4 (1997) 236–242.
[10] D. Zhong, S.K. Pal, D. Zhang, S.I. Chan, A.H. Zewail, Proc. Natl. Acad. Sci. 99 (2002) 13–18.
[11] B. Börger, D. Suter, J. Chem. Phys. 115 (2001) 9821–9826.
[12] Y. Xiao, H. Wang, S.J. George, M.C. Smith, M.W.W. Adams, F.E. Jenney Jr., W. Sturhahn, E.E. Alp, J. Zhao, Y. Yoda, A. Dey, E.I. Solomon, S.P. Cramer, J. Am. Chem. Soc. 127 (2005) 14596–14606.
[13] G. Hernández, F.E. Jenney Jr., M.W.W. Adams, D.M. LeMaster, Proc. Natl. Acad. Sci. 97 (2000) 3166–3170.
[14] G. Hernández, D.M. LeMaster, Biochemistry 40 (2002) 14384–14391.
[15] A. Grottesi, M.-A. Ceruso, A. Colosimo, A. Di Nola, Proteins: Struct. Funct. Genet. 46 (2002) 287–294.
[16] R. Bau, D.C. Rees, D.M. Kurtz, R.A. Scott, H.S. Huang, M.W.W. Adams, M.K. Eidsness, J. Biol. Inorg. Chem. 3 (1998) 484–493.
[17] K. Kurihara, I. Tanaka, T. Chatake, M.W.W. Adams, F.E. Jenney Jr., N. Moiseeva, R. Bau, N. Niimura, Proc. Natl. Acad. Sci. 101 (2004) 11215–11220.
[18] P.R. Blake, J.B. Park, Z.H. Zhou, D.R. Hare, M.W. Adams, M.F. Summers, Protein Sci. 1 (1992) 1508–1521.
[19] H.L. Fragnito, J.Y. Bigot, P.C. Becker, C.V. Shank, Chem. Phys. Lett. 160 (1989) 101–104.
[20] A.H. Zewail, J. Phys. Chem. A 104 (2000) 5660–5694.
[21] J.M. Jean, G.R. Fleming, J. Chem. Phys. 103 (1995) 2092–2100.
[22] A.E. Johnson, A.B. Myers, J. Chem. Phys. 104 (1996) 2497–2507.
[23] L. Zhu, P. Li, M. Huang, J.T. Sage, P.M. Champion, Phys. Rev. Lett. 72 (1994) 301–304.
[24] F. Rosca, A.T.N. Kumar, D. Ionascu, T. Sjodin, A.A. Demidov, P.M. Champion, J. Chem. Phys. 114 (2001) 10884–10898.
[25] R.A.G. Cinelli, V. Tozzini, V. Pellegrini, F. Beltram, G. Cerullo, M. Zavelani-Rossi, S. De Silvestri, M. Tyagi, M. Giacca, Phys. Rev. Lett. 86 (2001) 3439–3442.
[26] T. Cimei, A.R. Bizzarri, S. Cannistraro, G. Cerullo, S.D. Silvestri, Chem. Phys. Lett. 362 (2002) 497–503.
[27] T. Cimei, A.R. Bizzarri, G. Cerullo, S.D. Silvestri, S. Cannistraro, Biophys. Chem. 106 (2003) 221–231.
[28] A. Paciaroni, M.E. Stroppolo, C. Arcangeli, A.R. Bizzarri, A. Desideri, S. Cannistraro, Euro. Biophys. J. 28 (1999) 447–456.
[29] W. Doster, S. Cusack, W. Petry, Nature 337 (1989) 754–756.
[30] F.E. Jenney Jr., M.W.W. Adams, Method. Enzymol. 334 (2001) 45–55.
[31] B.R. Brooks, R.E. Bruccoleri, B.D. Olafson, D.J. States, S. Swaminathan, M. Karplus, J. Comput. Chem. 4 (1983) 187–217.
[32] R.B. Yelle, N.-S. Park, T. Ichiye, Proteins: Struct. Funct. Genet. 22 (1995) 154–167.
[33] J.T. Sage, S.M. Durbin, W. Sturhahn, D.C. Wharton, P.M. Champion, P. Hession, J. Sutter, E.E. Alp, Phys. Rev. Lett. 86 (2001) 4966–4969.
[34] B.M. Leu, M.Z. Zgierski, G.R.A. Wyllie, W.R. Scheidt, W. Sturhahn, E.E. Alp, S.M. Durbin, J.T. Sage, J. Am. Chem. Soc. 126 (2004) 4211–4227.
[35] W.R. Scheidt, S.M. Durbin, J.T. Sage, J. Inorg. Biochem. 99 (2005) 60–71.
[36] L.D. Book, D.C. Arnett, H. Hu, N.F. Scherer, J. Phys. Chem. A 102 (1998) 4350–4359.
[37] M.D. Edington, W.M. Diffey, W.J. Doria, R.E. Riter, W.F. Beck, Chem. Phys. Lett. 275 (1997) 119–126.
[38] R.S. Czernuszewicz, J. LeGall, I. Moura, T.G. Spiro, Inorg. Chem. 26 (1986) 696–700.
[39] M.J.J. Vrakking, D.M. Villeneuve, A. Stolow, Phys. Rev. A 54 (1996) R37–R40.
[40] T. Kobayashi, T. Saito, H. Ohtani, Nature 414 (2001) 531–534.
[41] M.R. Armstrong, J.P. Ogilvie, M.L. Cowan, A.M. Nagy, R.J.D. Miller, Proc. Natl. Acad. Sci. 100 (2003) 4990–4994.
[42] A.M. Nagya, V. Raicuc, R.J.D. Miller, Biochim. Biophys. Acta 1749 (2005) 148–172.
[43] S. Nakashima, Y. Nagasawa, K. Seike, T. Okada, M. Sato, T. Kohzuma, Chem. Phys. Lett. 331 (2000) 396–402.
[44] A.R. Bizzarri, A. Paciaroni, C. Arcangeli, S. Cannistraro, Euro. J. Biophys. 30 (2001) 443–449.
[45] C. Arcangeli, A.R. Bizzarri, S. Cannistraro, Biophys. Chem. 90 (2001) 45–56.
[46] D.E. Bennett, M.K. Johnson, Biochim. Biophys. Acta 911 (1987) 1–80.
[47] V.S. Oganesyan, S.J. George, M.R. Cheesman, A.J. Thomson, J. Chem. Phys. 110 (1999) 762–777.
[48] B. Brooks, M. Karplus, Proc. Natl. Acad. Sci. 80 (1983) 6571–6575.
[49] D.H. Jung, N.S. Kang, M.S. Jhon, J. Phys. Chem. A 101 (1997) 466–471.
[50] H. Saito, T. Imai, K. Wakita, A. Urushiyama, T. Yagi, Bull. Chem. Soc. Jpn. 64 (1991) 829–836.
[51] T. Iwasaki, A. Kounosu, D.R.J. Kollling, A.R. Crofts, S.A. Dikanov, A. Jin, T. Imai, A. Urushiyama, J. Am. Chem. Soc. 126 (2004) 4788–4789.
[52] F.A. Rotsaert, J.D. Pikus, B.G. Fox, J.L. Markley, J. Sanders-Loehr, J. Biol. Inorg. Chem. 8 (2003) 318–326.
[53] G. Cerullo, S.D. Silvestri, Rev. Sci. Instrum. 74 (2003) 1–18.